Lunar Augmented Navigation Service Interoperability Demonstration - Reference Products and Expected PVT Accuracy

Floor T. Melman, *European Space Agency*
Richard D. Swinden, *European Space Agency*
Jillian S. Oduber, *European Space Agency*
Yoann Audet, *European Space Agency*
Cosimo Stallo, *European Space Agency*
Cheryl J. Gramling, *National Aeronautics and Space Administration*
Juan M. Crenshaw, *National Aeronautics and Space Administration*
Masaya Murata, *Japan Aerospace Exploration Agency*
Suzuna Okamoto, *Japan Aerospace Exploration Agency*
Javier Ventura-Traveset, *European Space Agency*
Serena Molli, *European Space Agency*

BIOGRAPHIES

Floor T. Melman received his MSc in Aerospace Engineering at the Delft University of Technology in 2018. He is currently a navigation systems engineer in the navigation system definition section within ESA/ESTEC in the Netherlands. He is coordinating the GNSS receiver experiment that will fly on the Lunar Pathfinder mission and supports the ESA Moonlight program that will provide lunar communication and navigation services. Furthermore, he is the ESA lead within the LunaNet PNT working group that will define standards and protocols enabling interoperable lunar PNT systems.

Richard D. Swinden is a Navigation System Engineer in the E2E Systems Division at ESA. His current responsibilities involve providing system and navigation engineering support to lunar and Mars-related projects including Moonlight, Argonaut and LightShip-MARCONI. He holds a first-class Master of Electronic Engineering degree from the University of Nottingham and has more than 15 years of experience in the GNSS and space domains.

Jillian S. Oduber is currently a Young Graduate Trainee in the Future Navigation Department at ESA. She holds an MSc in Aerospace Engineering from the Delft University of Technology, where she specialized in Space Flight, and more specifically on topics such as GNSS and precise orbit determination. In her current role at ESA, she supports Lunar and Martian navigation projects through simulations on user PVT performance, and orbit determination and time synchronization.

Yoann Audet received his MSc in Aerospace Engineering from Institut Polytechnique des Sciences Avancees (IPSA) in 2021 and his advanced master in Space Applications and Services (SPAPS) from ISAE-SUPAERO in 2022. He joined ESA in 2022 as a Young Graduate Trainee to support interplanetary navigation projects such as Moonlight, LightShip-MARCONI and ArgoNET/NovaMoon.

Cosimo Stallo got an MSc in Electronic Engineering at the Polytechnic of Bari (2005), Master of Science Post-lauream on Advanced Satellite Communications and Navigation Systems (2006) and finally a PhD in Microelectronics and Telecommunications at the University of Rome Tor Vergata (2009) cum laude. He has almost 20 years of experience in sat telecommunication and navigation working in Academia, Agency (ASI and ESA) and Industry (TAS).
He joined TAS Italy in Dec 2019 as Senior System Navigation Engineer. In March 2023 he was appointed Head of Unit on E2E system design within Navigation Systems Department in Domain of Observation and Navigation. In June 2024 he joined ESA as LCNS/Moonlight Principal Navigation System engineer.

Cheryl J. Gramling is the Cislunar Strategist and PNT Lead at NASA Headquarters Space Communications and Navigation. She is a Goddard Senior Fellow with over 40 years experience in trajectory design, navigation, and timing for NASA missions across all orbital regimes, including relays and distributed system missions. She currently leads NASA's communications and position, navigation, and timing for lunar missions, including multi-lateral developments and standards.

Juan M. Crenshaw is a Navigation Engineer at NASA's Goddard Space Flight Center since 2020. He has over 15 years of prior experience with communications networks and spacecraft navigation, holding telecommunications engineering degrees from UPM, UAX (Spain). Juan is involved in technology development for lunar position, navigation, and timing, and is dedicated to promoting interoperable solutions, including the development of standards such as LunaNet. Additionally, Juan is involved in international organizations, including International Committee on GNSS (ICG) and the Consultative Committee for Space Data Systems (CCSDS).

Masaya Murata joined the Japan Aerospace Exploration Agency (JAXA) in 2017 and he is currently the lunar PNT lead for Japan lunar PNT system called Lunar Navigation Satellite System (LNSS). He has a ten-year private-company experience prior to joining the JAXA and earned his Ph.D. from the University of Tokyo in 2017. From October 2021 to September 2022, he served as a visiting scholar at the Aalto university in Finland and the University of Texas at Austin in U.S., respectively. He is now actively participating in the International Committee on GNSS (ICG) and the Interagency Operations Advisory Group (IOAG) to facilitate the international collaboration for the lunar PNT.

Suzuna Okamoto joined the Japan Aerospace Exploration Agency (JAXA) as an engineer in 2024. She belongs to the lunar PNT team and is in charge of the consideration for lunar reference frames and time frames. She received her MSc in aeronautics and astronautics at the University of Tokyo.

Javier Ventura-Traveset has worked more than 35 years at the European Space Agency (ESA). He is the Moonlight Project Navigation Manager and Navigation Science Manager, managing all ESA lunar navigation-related activities, including the ESA Lunar Pathfinder, Moonlight and NovaMoon programs. He also coordinates all ESA GNSS scientific-related activities and serves as the Executive Secretary of the ESA GNSS Scientific Advisory Committee. He is an Academician at the Royal Academy of Engineering of Spain

Serena Molli is a Postdoctoral Researcher in the Navigation Support Office at ESA–ESOC, working on interplanetary navigation and GNSS positioning for projects such as *Moonlight* and *Lunar Pathfinder*. She received her MSc *cum laude* in Space Engineering from Sapienza University of Rome in 2020 and her PhD on Martian and Lunar Navigation Systems from the same institution in 2023. During her doctoral studies, she undertook a secondment at ESA–ESTEC, contributing to *Moonlight* and *MARCONI*. Her research focuses on advanced navigation concepts for future lunar and planetary exploration.

ABSTRACT

Currently, NASA, ESA, and JAXA are defining the LunaNet Interoperability Specification (LNIS). This specification will enable interoperable communication and Position, Navigation, and Timing (PNT) services on the Moon. Within the LunaNet framework, the Lunar Augmented Navigation Service (LANS) aims to provide Regional Navigation Satellite Systems (RNSS)-like services to lunar users (i.e., rovers, landers, and orbiters). The service will be provided by different LunaNet service provider (LNSP) nodes each broadcasting the Augmented Forward Signal (AFS) to form regional coverage with appropriate geometry.
Currently, ESA, NASA, and JAXA are developing LunaNet instantiations with industrial partners; respectively, Moonlight Lunar Communication and Navigation System (LCNS), Lunar Communication Relay and Navigation System (LCRNS), and Lunar Navigation Satellite System (LNSS) that each contribute to the LANS. By 2029, the first five nodes (1 LCNS node, 3 LCRNS nodes, and 1 LNSS node) are planned to be in lunar orbit broadcasting the AFS and thus contributing to the LANS. Along with the LNSS satellite and the demonstration payload including the LANS receiver to be delivered to the Moon, JAXA is planning to perform a joint ESA-JAXA-NASA LANS interoperability demonstration.

This mission will aim to:
1) Acquire and track in-situ AFS signals from all LNSP nodes and assess the signal quality.
2) Estimate the signal-in-space error (SISE) of each LNSP node.
3) Demonstrate the interoperable approach is viable for a user to produce their position, velocity, and time (PVT) estimate.
4) Perform additional experiments concerning, among others, lunar time and reference systems.

To this end, the lander aims to embark a set of LANS receivers, an atomic clock (e.g., MiniRAFS), a laser retroreflector, and a Tracking, Telemetry, and Command (TT&C) transponder for Direct with Earth (DWE) communication and ranging.
Due to the availability of precise geodetic techniques (e.g., a laser retroreflector), the position of the lander should be well surveyed providing a high-accuracy reference location. This reference position should enable the validation of the PVT solution achieved through combined usage of the LNSPs by NASA, ESA, and JAXA and thus demonstrate interoperability as achieved

at the AFS level for the user. Moreover, when the precise a-posteriori LNSP products are available (similarly to GNSS precise products), the UERE (User Equivalent Ranging Error) can be characterized which should enable the estimation of the LNSP SISE.
Moreover, having precise PVT, a stable, free-running atomic clock, and time-transfer capabilities could support the characterization of relativistic offsets between Moon- and Earth-based clocks. Furthermore, as part of the interoperable PVT, the impact of the different system time realizations of each LNSP and the provided offsets to relate back to LunaNet Reference Time (LRT) can be assessed. Finally, the presence of the lunar laser retroreflector (LRR) can support further improvements of the lunar reference frame realizations.

This paper will analyze the different aspects of the LANS interoperability demonstration mission. First, it will simulate the accuracy of the reference PVT that can be achieved with the embarked geodetic techniques. Secondly, a preliminary assessment of the accuracy of the interoperable user PVT will be provided. This assessment will consider the latest information concerning the LNSP orbits and system design parameters (e.g., SISE). Finally, this paper aims to characterize the accuracy with which the reference user clock offset can be obtained by adding GNSS receiver capabilities on the lander.

1. INTRODUCTION

1.1. LunaNet

LunaNet is a framework [1] for interoperable lunar communications and position, navigation, and timing (C&PNT) services based on standards, interfaces, and protocols identified in the LunaNet Interoperability Specification (LNIS) document set [2] jointly developed by NASA, ESA, and JAXA. The vision is to establish the operational basis at the Moon for an internet-like data transport service and accurate in-situ PNT service, both suitable for future scalability across the solar system. The interoperable C&PNT services align with the Moon-to-Mars objectives [3] for lunar infrastructure and the recurring tenet for technical and operational interoperability across mission elements.

1.2. LANS and Augmented Forward Signal

LunaNet navigation services are primarily provided through the Augmented Forward Signal (AFS) [2]. The AFS is a GNSS-like signal (i.e., in terms of modulation) which will be broadcast by LunaNet Service Provider (LNSP) nodes in the S-band frequency (2492.028 MHz). Similar to GNSS, at least 4 signals transmitted by independent LNSP nodes are required to derive an instantaneous position, velocity, and time (PVT) solution. However, other sensors (such as Inertial Measurement Units (IMUs), Digital Elevation Models (DEMs), etc. can be used to derive PVT at user level with less than 4 satellites. In case 4 LNSP nodes (either from one or multiple LNSPs) transmit AFS simultaneously, a concept called the Lunar Augmented Navigation Service (LANS) is realized. The AFS will also carry a navigation message that enables users to obtain Clock and Ephemeris Data (CED) that are fundamental to derive a PVT solution.

Figure 1 shows a realization of the LANS during the LANS interoperability demonstration mission, which would take place in 2029. This figure represents the orbits of the ESA Moonlight LCNS IOC (Initial Operational Capability) node, the NASA LCRNS IOC-B nodes, and Japan LNSS demonstration mission node. Assumptions for this study on the orbital elements of these nodes are further detailed in Table 3.

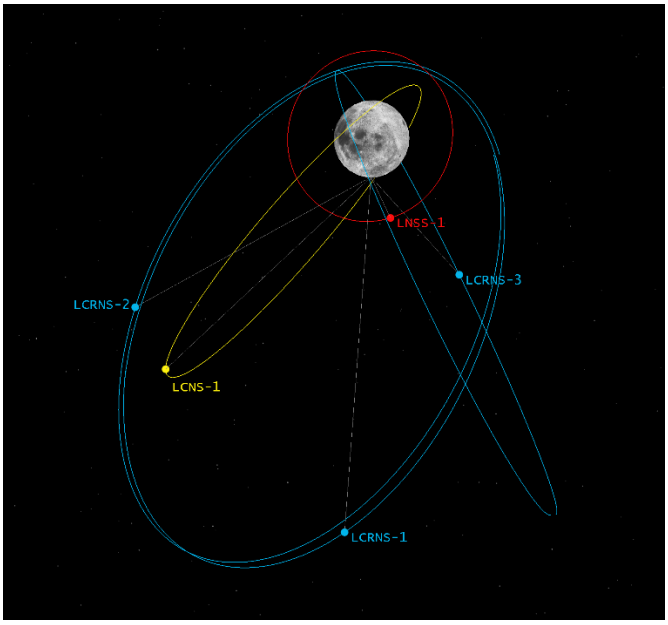

Figure 1 - Lunar PNT services provided by international LNSPs (ESA's LCNS, NASA's LCRNS, and Japan's LNSS). This figure represents the situation in 2029 during the LANS interoperability demonstration. Note that the orbits are notional and further detailed in Table 3.

To ensure interoperability among the various LNSPs, it is fundamental that the CED refer to a common reference frame and timescale. The reference frames and timescale to be adopted by LunaNet are currently being defined and will be documented in Applicable Document (AD) LNIS [2] AD-5.

1.3. LunaNet Service Provider Descriptions

1.3.1. ESA's Moonlight LCNS

ESA is currently developing the Moonlight Lunar Communication and Navigation System (LCNS). The LCNS consists of five satellites: four navigation satellites and one communication satellite. The first navigation satellite and the communication satellite will be launched in 2029 declaring Initial Operational Capability (IOC), while the remaining three navigation satellites will be launched in 2030 declaring Full Operational Capability (FOC). The navigation satellites will be located in 24-hour Elliptical Lunar Frozen Orbits (ELFO). In this way, through broadcasting the LunaNet AFS, users within the lunar South Pole should be able to derive PVT for at least 15 hours per day. By the time of the LANS demonstration mission, LCNS is expected to be at IOC (one navigation and one communication satellite).

1.3.2. NASA's Lunar Communications Relay and Navigation System (LCRNS)

LCRNS is a NASA Space Communications and Navigation (SCaN) Project within the Goddard Space Flight Center. LCRNS addresses relay-based communication and positioning requirements for NASA's lunar mission stakeholders throughout the Moon-to-Mars Artemis Program. While LunaNet establishes the cooperative framework for interoperable lunar orbiting C&PNT infrastructure, LCRNS specifically defines and validates its requirements for the commercial services implementing this capability. The LCRNS relay services respond to a three-phased deployment that meets NASA's evolving C&PNT needs in the lunar South Pole Service Volume. Initial Operating Capability-Charlie (IOC-C) requires a minimum of four AFS links in view meeting a Geometric Dilution of Precision (GDOP) less than six for 40% of an Earth day. Each LCRNS AFS must meet a position Signal in Space Error (SISEpos) of 13.43m, 3σ. By leveraging commercial services, LCRNS represents a sustainable approach to human and robotic exploration infrastructure that aligns with broader Moon-to-Mars objectives. For the demonstration, NASA expects LCRNS to have AFS transmitted from three different lunar orbital nodes, which will also provide communication services.

1.3.3. Japan's LNSS

The Lunar Navigation Satellite System (LNSS) is a Japanese lunar PNT system under development, aiming to provide a high-accuracy positioning and navigation service at the lunar South Pole region. The first LNSS satellite is expected to be launched in 2029 to demonstrate its onboard technologies of GNSS weak signal navigation and navigation signal (AFS) generation and

broadcasting. The mission will simultaneously validate the broader LNSS system through ground-based AFS reception by the LANS receiver positioned at the lunar South Pole region, while evaluating overall system performance including Signal-In-Space Error (SISE) and PVT solution accuracy in the actual lunar environment. The baseline LNSS satellite constellation is composed of eight navigation satellites to be deployed in two stable orbits called the Elliptical Lunar Frozen Orbits (ELFOs) [4]. The actual satellite orbits and the total number of satellites are subject to change, as the system development proceeds. The LNSS complies with the LNIS to become interoperable with the other LNSPs and together forms the LANS by broadcasting the AFSs towards lunar users. By the time of the demonstration, Japan expects to have a first LNSS (demonstration) satellite deployed in a circular lunar polar orbit, transmitting only the AFS.

1.4. LANS Interoperability Demonstration Mission

Interoperability is critical to the LANS. The current concept is to combine different LNSP space vehicles to create a constellation of AFS broadcasters that form LANS. To demonstrate the interoperability between the LNSPs, JAXA is proposing the first-ever LunaNet LANS interoperability demonstration mission in 2029 by deploying the first LNSS (demonstration) satellite in the Moon orbit and the LANS receiver at the lunar South Pole region. In 2029, three NASA LCRNS satellites (representing IOC-B) and one ESA LCNS satellite are expected in their respective ELFOs and together with the LNSS satellite, will enable demonstration of the LANS interoperability by receiving their AFSs with the LANS receiver to be placed on the lunar surface. The outcomes of this mission will prove the capability of the LANS concept and pave the way toward operational deployment of the LANS in 2030s.

2. DEMONSTRATION MISSION

2.1. Mission Objectives

The objective of the LANS demonstration mission is to validate the end-to-end performance of the first instance of LANS, which is comprised by one Japanese LNSS node, one ESA LCNS PNT node, and at least two NASA LCRNS nodes. To achieve this, the demonstration lander will carry at least two LANS receivers to acquire, track, and process the broadcast AFS by the different LNSP nodes contributing to the LANS. In this way, the lander enables the verification of the interoperability between the different LNSPs. The demonstration lander will also carry a set of geodetic technique payloads (which are further detailed in Section 3) which will enable a precise estimation of the lander's position and time, which can be used as a reference to benchmark the LANS derived PVT solution.

The objectives of the LANS demonstration mission (presented in [5]) are recalled below:

1. To receive AFS from each LSNP node and assess the signal quality.
2. To compute and validate the SISE for each LNSP node by:
    a. Estimating the LNSP node orbit SISE contribution
    b. Estimating the LNSP node clock SISE contribution
    c. Evaluate contributing errors (e.g., LNSP node hardware delays)
3. To validate the achieved user Position, Velocity, and Time (PVT) knowledge from the combined LANS:
    a. To estimate the User Equivalent Ranging/Range Rate Error (UERE/UERRE) per LNSP node
    b. To estimate the different user Dilution of Precision (DOP) metrics
4. To validate the LunaNet Time and Reference Frame

A detailed description on how each of these objectives is met is provided in [5]. This publication covers the following aspects related to the objectives:

- The derivation of the "truth" position of the lander which will be used to characterize the performance of the LANS-based PVT solution. Section 3 covers the instruments that are used to derive this "truth", while Section 5.1 provides an estimate on the attainable precision of the "truth". This "truth" solution is subsequently used within objectives 2 and 3 as detailed in [5].
- The derivation of the "truth" time through GNSS time transfer as described in Section 5.3. This reference time will be subsequently used within objectives 2 and 3 as detailed in [5].
- A first iteration (compared to the results presented in [5]) on the attainable LANS-based PVT solution considering the latest representative orbits for LCRNS. This relates to objective 3.

2.2. Mission Architecture

Figure 2 depicts the architecture plan for the LANS interoperability demonstration mission. The JAXA-ESA-NASA LANS interoperability demonstration mission, currently targeted for 2029, aims to contribute to verifying interoperability of the available AFS broadcast by the different provider satellites. Placing the LANS receiver(s) at the lunar South Pole (SP) region enables the characterization of AFS broadcast by these LNSP nodes, in order to verify interoperability among these lunar PNT systems in an overlapping service area. Although still under investigation, the lander is expected to include one laser retroreflector (LRR) and one miniature Rubidium Atomic Frequency Standard (MiniRAFS) to enable the determination of the lander's "true" position and clock reference. By using these assets, the achieved SISE associated with each LNSP satellite, along with the joint LANS PVT performance, will be evaluated by exchanging relevant data between the three space agencies (ESA, JAXA, and NASA).

The mission data acquisition and concept for the evaluation of the "truth" data are illustrated in Figure 3. On the left of Figure 3, the mission data refer to the in-situ data consisting of the received AFS raw measurements and the LANS receivers' PVT solutions. Furthermore, the LNSP node mission data includes observations, clock, and ephemeris solutions from each node. For example, the LNSS node mission data includes observations from GNSS weak signals received by the LNSS satellite. As applicable, this mission data will be transmitted to Earth ground stations via the data transmission link of the LNSP node, the lander's data transmitter, or using other available lunar relay nodes such as ESA's Lunar Pathfinder.

As illustrated on the right of Figure 3, the "truth" data are composed of the LNSP node precise orbit and onboard clock data (similar to GNSS precise products) and the LANS receiver's precise position and clock data. The "truth" data will be used to validate the LANS receiver interoperable PVT and the SISE of the LNSP nodes. The LNSS satellite precise orbit will be determined by using traditional X-band DWE ranging and Delta-Differential One-way Ranging (DDOR), while the LCNS satellite precise orbit will be determined using X-band DWE ranging (like the real-time products[1]) and LLR (only occasionally). Then, based on the precise orbit determination results, the LNSS satellite clock data will be estimated by using the downlinked LNSS observations from GNSS weak signals received, while for the LCNS satellite, the clock offset will be estimated by two-way satellite time-transfer (like the real-time products[1]). Methods for obtaining independent reference orbit and clock determination approaches for the demonstration for the LCRNS satellites are under investigation. The precise LANS receiver's position will be determined based on terrestrial based ranging (i.e., DWE ranging, Delta-Differential One-Way Ranging (DDOR), and LLR) as further detailed in Section 5.1. Then, based on these precise position results, the receiver clock offset may be estimated by either 1) post-processing of LANS data, 2) GNSS based time-transfer (as detailed in Section 5.3), or 3) two-way time-transfer using the DWE link. The actual method for precise characterization of the receiver clock offset is still under investigation.

[1] The main difference between the real-time and a-posteriori products for Moonlight LCNS, are that the precise products do not require propagation which means they are more accurate.

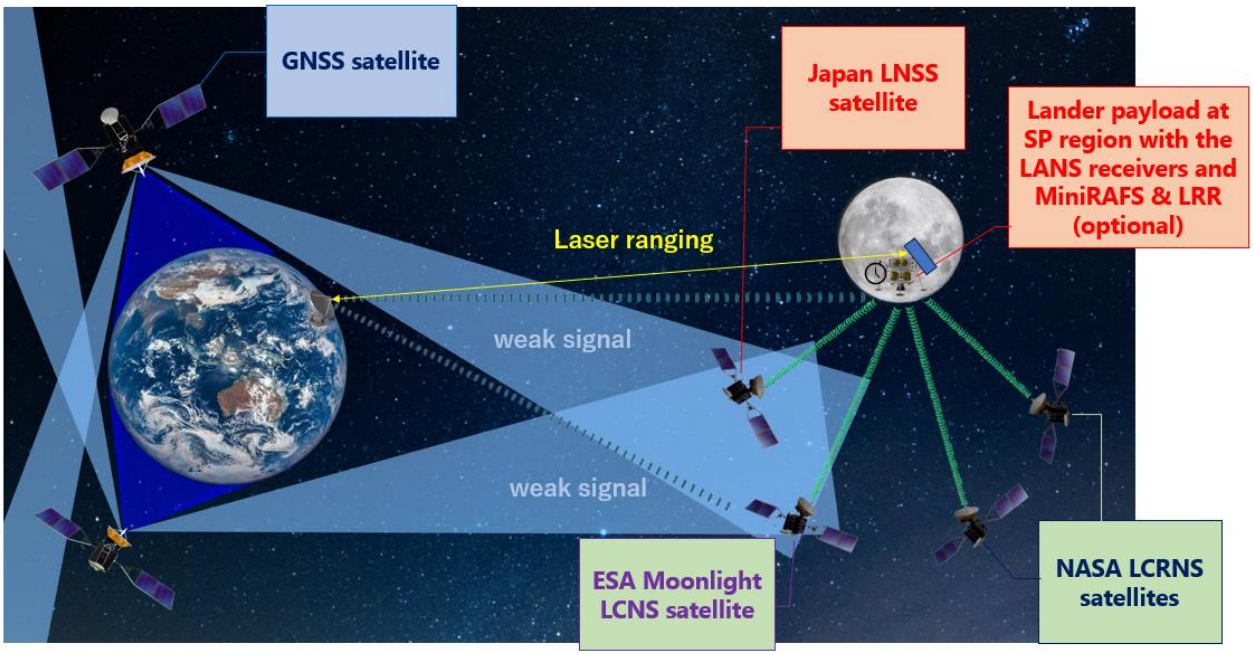

Figure 2 - LANS interoperability demonstration architecture plan.

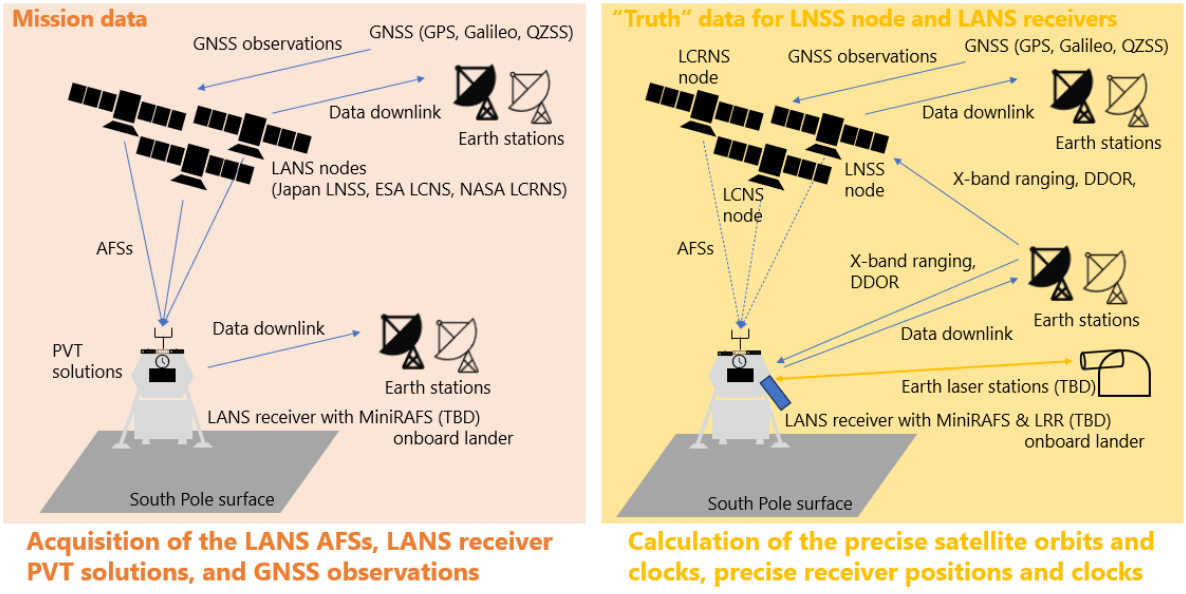

Figure 3 - Mission data acquisition and "truth" data calculation.

3. MISSION PAYLOADS

To fulfill the mission objectives, the following payloads are being considered for the LANS demonstration mission, which are further detailed in the subsequent sections (noting that the list of payloads is not confirmed yet):

- LANS Receiver(s) with internal OCXO
- GNSS Receiver
- MiniRAFS
- Laser Retroreflector (LRR)
- TT&C System (for DWE tracking and communications)

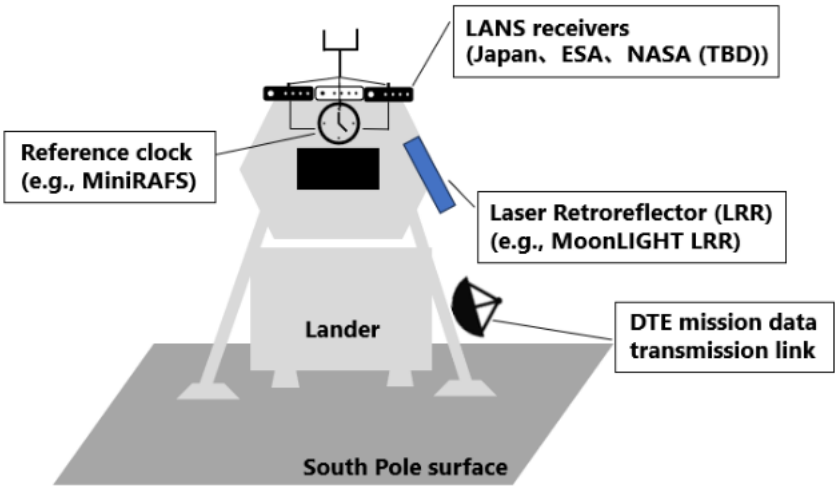

Figure 4 - Demonstration lander with the identified payloads.

3.1. LANS Receivers

Linked to objectives: Obj-1, Obj-2, Obj-3

The demonstration lander will carry at least two LANS receivers (one developed by JAXA and one by ESA) and potentially a third receiver developed by NASA. The LANS receivers are used to acquire, track, and decode the AFS broadcasted by the various LNSP nodes. Each of the LANS receivers will likely have an internal clock such as an OCXO and will have an interface (through a splitter) to an external MiniRAFS (see Section 3.3.1) as shown in Figure 5. This would enable validation of the LANS-based user clock estimation against the stable MiniRAFS time which can be linked to UTC through time transfer techniques such as GNSS and/or two-way time-transfer through the DWE link.

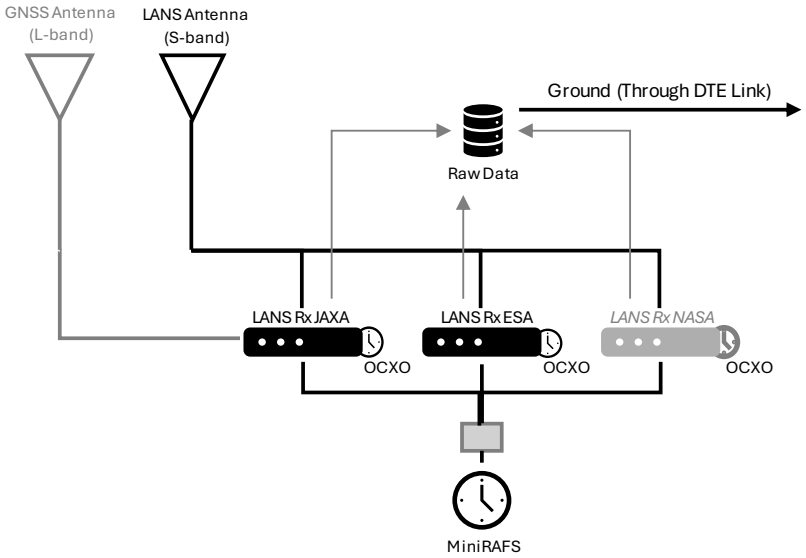

Figure 5 - Schematic diagram of the receiver architecture. The block between the MiniRAFS and the receivers represents a splitter.

Each LANS receiver would also have an on-board PVT engine that would enable the receiver to evaluate a LANS-based PVT solution. Furthermore, each receiver would store the raw data (i.e., PVT, pseudorange, Doppler, etc.) which would be downlinked to Earth for further analysis (i.e., SISE validation and signal quality assessment).

3.2. GNSS Receiver

Linked to objectives: Obj-2, Obj-3

The GNSS receiver is not baselined but is an option that could be used to perform time-transfer. When the position of the lander is known accurately (through DWE range and Doppler measurements as well as LLR and DDOR), GNSS measurements provide direct access to the respective GNSS system time (and thus to UTC through the disseminated or post-processed GNSS to UTC timing offsets). Due to the low received power at lunar distances [6], a high-sensitivity receiver will be required. Furthermore, either a low-gain or high-gain antenna could be used. The advantage of a low-gain antenna would be the low size, weight, and power (SWaP), and the fact that no Antenna Pointing Mechanism (APM) would be required. However, in this configuration, only the main lobes could be tracked. Alternatively, a high-gain (e.g., +15 dBi) antenna could be used which would also enable tracking of the GNSS signals through the secondary lobes, thus increasing the number of available satellites. However, due to the narrow beamwidth, this type of antenna will need an APM to point the antenna in the right direction or rely on sufficient lander orientation control during landing.

To avoid the need to equip the lander with another receiver unit, the GNSS functionality could be added to the LANS receiver. Each channel would then be generic and could be allocated to both an LNSP or GNSS node. However, as the carrier frequency is different between LANS and GNSS (S-band versus L-band), some modifications of the front-end are needed, considering either:

- A dedicated RF front-end for GNSS L-band signals on top of the S-band RF front-end (as shown in Figure 5).
- A single front-end with dedicated RF paths to accommodate both LANS and GNSS.
- An additional front-end module which down converts the S-band signals to the L-band. Subsequently, all signals are further processed by a dedicated L-band front-end. Given the diversity of the codes (and the fact that LunaNet does not use codes currently in use by GNSS systems) signals could be differentiated by their unique PRN codes.

More details on the time-transfer accuracy that can be realized with GNSS can be found in Section 5.3.

3.3. On-Board Clock

As indicated in Section 3.1, each LANS receiver would have an internal OCXO and would, on top of that, have an interface to a common MiniRAFS (that is shared among all receivers). Section 3.3.1 provides more detail on the MiniRAFS while Section 3.3.2 provides some details on the internal OCXO.

3.3.1. MiniRAFS

Linked to objectives: Obj-1, Obj-2, Obj-3, Obj-4

A miniature Rubidium Atomic Frequency Standard (MiniRAFS) is a space-qualified atomic clock developed by Safran Navigation & Timing [7] for space applications. The clock is a miniaturized version of the RAFS (Rubidium Atomic Frequency Standard) and has a mass of 0.45 kg and a power consumption of 10 to 15 W.

The MiniRAFS can be used to provide a stable timing reference to which the LANS interoperable PVT can be compared. Furthermore, it would provide a stable reference frequency for signal quality monitoring. Finally, when operated for enough time and when the clock ticks at its proper time, it may contribute to lunar timing experimentation by measuring the relativistic effects of a clock ticking on the Moon. This, however, depends on the duration of the mission (i.e., given the stability of the MiniRAFS, the relativistic effects are only observed after a certain period) and is part of further investigations.

3.3.2. OCXO

Linked to objectives: Obj-3

A space-grade OCXO could be used as the internal clock for each LANS receiver. In this way, it adds redundancy to the MiniRAFS and would also make the receiver more representative of a typical lunar user that would not be equipped with a MiniRAFS clock. A representative product is the Iris OCXO developed by Bliley Technologies [8], which has a mass of 16 grams and a power consumption of 1.5 to 3.0 W. The characteristics of this clock, including some additional assumptions, have been used for the GNSS time transfer analysis, resulting in the OCXO clock model given in Table 6.

3.4. Laser Retroreflector

Linked to objectives: Obj-2, Obj-3, Obj-4

A laser retroreflector (LRR) can be used to reflect photons sent by terrestrial laser ranging stations (such as the Grasse and Apache Point stations). In this way, very precise range measurements (at an accuracy of centimeter level [9]) can be obtained. It is important that the optical axis of the laser retroreflector (LRR) is pointed to the mean Earth direction. This can be realized through an APM (potentially shared with the GNSS antenna) or by ensuring the lander is oriented in the right direction.

3.5. DWE Link

Linked to objectives: Obj-2, Obj-4

An X or K/Ka band (TBC) DWE transponder placed on board of the JAXA lander can be used for TT&C functionality and support ranging and two-way time transfer (TBC) functionalities with Earth ground TT&C stations.
The DWE transponder allows to acquire range and Doppler measurements contributing together with on-board LRR to accurately estimate the position of the lander on the lunar surface and can establish a (TBC) two-way measurement session with the visible TT&C station determining the time offset between the lander on-board clock and the LNSP System Time, that can be continuously observed and monitored.
The DWE transponder, together with the other instruments on board (LRR, DDOR), enables generating the "truth" position of the lander to compare it with what can be achieved through the LANS based PVT solution and to monitor the stability of MiniRAFS timing reference to which the LANS interoperable PVT can be compared.

4. IMPROVEMENT OF LUNAR REFERENCE FRAMES

There is a possibility that the LANS demonstration mission payloads contribute to the improvement of lunar reference frames. The retroreflectors carried to the Moon surface during the Apollo missions and the Luna missions are utilized to realize lunar body-fixed reference frames such as Principal Axis (PA) system and Mean Earth (ME) system. The location where the retroreflector of this mission will be placed will become a new additional reference point. Therefore, it will contribute to improving the precision of reference frame realization and maintenance.

5. PRELIMINARY ANALYSIS

5.1. Lander Reference PVT Accuracy

The "truth" data should be precise enough to be able to fulfill the mission objectives (i.e., validation of LANS-based PVT and LNSP node SISE characterization). The position accuracy requirements for the "truth" data are set to 3 meters RMS in each axis for the LANS receiver, although the goal is to achieve the one-meter-level accuracy. This level of accuracy is needed to enable the SISE evaluation of the LNSP nodes as well as the real-time PVT performance. For the LANS receiver clock, the accuracy requirement is set to 2 meters RMS with a goal of achieving the one-meter-level accuracy. As mentioned in Section 2.2, the position of the lander on the Moon surface at the lunar South Pole region will be determined by DWE ranging, DDOR, and lunar laser ranging (LRR). Then, the accuracy of the LANS receiver clock will be determined by continuously processing the received AFSs during the mission given the determined receiver position, or optionally through two-way time-transfer or GNSS time-transfer.

The following observation schedule and measurements accuracy was assumed for the determination of the lander precise position as shown in Table 1.

Table 1 - Observation Availability for the "truth" Position Determination of the Lander.

Measurement Type	Jitter	Bias	Observation Availability
Range	1 meter	20 meters	Every 60 seconds
Doppler	0.5 mm/s	n/a	Every 60 seconds
DDOR	100 psec	n/a	Every 720 sec
LLR	5 cm	5 cm	Every 720 – 5400 sec

For the analysis, it was assumed the use of one Range and Range Rate (RARR) station in Japan, one DDOR station in New Zealand paired with the Japanese RARR station for the North-South measurements, one DDOR station in Europe paired with the Japanese RARR station for the East-West measurements, and three laser ranging stations in Europe. Under this configuration, analysis shows that position accuracy of the LANS receiver can be on the order of 3 meters, provided laser ranging data were available: either 9 hours per day from a single station (Grasse) or 2 hours per day from 3 different stations (Grasse, Wettzell, Matera). This level of accuracy was assessed while assuming an error of approximately 3 meters on the knowledge of lunar ephemerides, by using two different sets of JPL DE ephemerides in the simulation and estimation process. The three-meter-level accuracy was observed for the LANS receiver position in each axis in this configuration. It was also found that the laser ranging data was necessary to achieve this level of position determination accuracy. The one-meter-level accuracy, however, could not be achieved and for better accuracy, it is necessary to reduce any lunar ephemeris and reference frame errors.

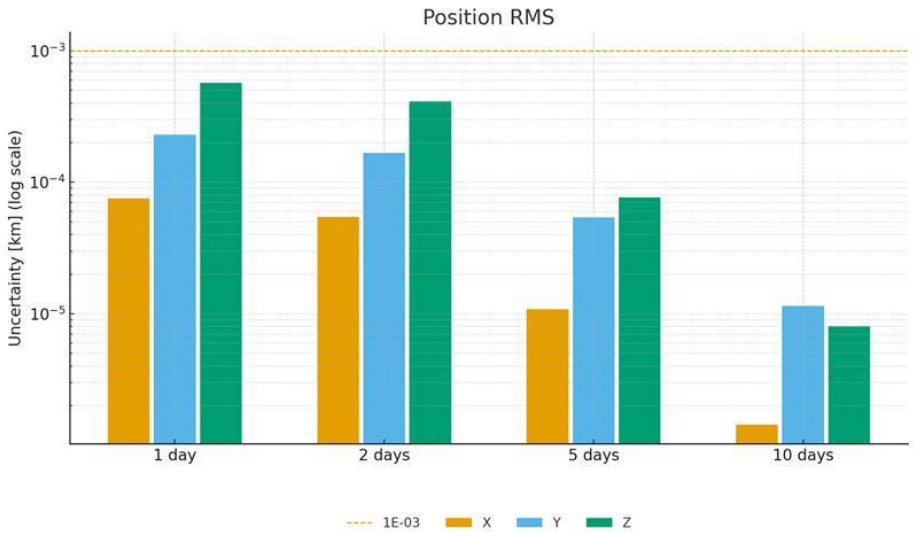

Figure 6 - 3D lander reference position accuracy.

Figure 6 shows that sub-meter uncertainty in the reference position can be achieved, provided that reference frame errors are not taken into account, across four different mission durations. In earlier results, these errors were assumed to be in the order of 3 meters [10], which was translating almost directly into the lander position error. This means that we have identified the techniques and scheduling strategies that allow the target accuracy to be reached, in order to isolate error contributions, but the reference frame remains the leading error source. Consequently, even for longer mission durations (up to 10 days), where the techniques alone would normally yield improved results, the accuracy is still limited by this bias (which is considered as a conservative approach, since the error in the ephemerides can be expected to be reduced to 1 meter in post processing ([10]). In other words, once the measurement techniques are optimized, the dominant source of error is no longer the technique itself but the underlying reference frame.

5.2. LANS Expected PVT Performance

The current work presents an updated analysis of the work presented previously by joint analysis from the agencies [5]. The results presented in this section are derived using a software suite, relying on a framework built around an Extended Kalman Filter (EKF). The software enables the processing of LANS measurements to solve for the position, velocity, and time of the user. The filter utilizes pseudorange measurements tightly fused with a Digital Elevation Model (DEM) for enhanced accuracy. The expectation and dispersion operators, as well as the kinematic propagation model, are presented in previous work [5].

The measurement model relies on the following assumptions:

- The noise of the pseudorange observable is modelled based on the thermal noise of a DLL (Delay Lock Loop) as modelled in [11].
- The SISE of the Moonlight navigation satellite is based on the method presented in [12].
- The SISE of the NASA and JAXA satellites is represented following the modelling method presented in [13] with tuned parameters to be representative of the expected performance and within the 20-meter (95 %) SISE target. Equation (1) presents the First-Order Gauss-Markov Process PSD (Power Spectral Density) model used for generating the SISE timeline of the NASA and JAXA systems.

$$S(f) = \frac{2{\sigma_b}^2/\tau_b}{1/\tau_b^2 + 4\pi^2 f^2} \quad (1)$$

Here, τ_b is the time constant of the Gauss-Markov process, σ_b is its standard deviation, and f is the frequency of the PSD. For this simulation, the frequency is assumed to be truncated between 10^{-6} and 10^{-2} Hz. Indeed, from [13], higher frequencies are not relevant for simulating the SISE performances of a GNSS system. The same assumption is taken for the lunar navigation system. As there is no actual data to determine the model parameters, the parameters are derived from analysis performed for Galileo and GPS [13] and adapted to the lunar case. Once simulated or real data is available for the JAXA and NASA ODTS (Orbit Determination and Time Synchronization) concepts, the model can be updated to fit closer to the operational concept. Table 2 provides the parameters to compute the PSD of the Gauss-Markov process and generate the time series of the SISEpos for each satellite. These parameters are tuned such that the generated noise from the PSD has a standard deviation matching the requirements presented in Table 3.

Table 2 – Simulation Parameters for the ODTS generation process.

		τ_b	σ_b
JAXA LNSP Nodes	**Position**	5h	7 m
	Clock	5h	3 m
NASA LNSP Nodes	**Position**	5h	4 m
	Clock	5h	1 m

The simulation parameters for each LNSP node are presented in Table 3. The configuration of the user (i.e., user antenna pattern, etc.) is similar to the configuration reported in [5]. The user is located at the lunar South Pole at the 88°S, 11.4°E (ICRF). The height for the given location is extracted from the LOLA DEM [14]. Furthermore, it is assumed that the user will be equipped with a LANS receiver [5] and a MiniRAFS clock.

Table 3 - Assumptions for the simulation of the LANS satellites. It should be noted that the orbits and EIRP are notional and are only applicable for a preliminary performance analysis within the context of this publication.

	ESA Moonlight LCNS Nav #1	**Japan LNSS Demo**	**NASA LCRNS #1**	**NASA LCRNS #2**	**NASA LCRNS #3**
Semi-major axis [km]	9748.14	3870.00	11999.2626	12027.7960	11993.3508
Eccentricity [-]	0.70	0	0.655	0.641	0.721
Inclination [deg]	48.04	104.428	32.22	31.33	79.07
Arg. of perilune [deg]	123.60	90.0	75.96	76.14	68.18
RAAN [deg]	89.49	53.563	-162.33	-164.02	-42.86
True anomaly [deg]	90.0	-5.0	-147.49	151.30	-119.79
Reference frame	ICRF	ICRF	ICRF	ICRF	ICRF
Epoch	2027-01-01 00:00:00.000 (TDB)	2027-01-01 00:00:00.000 (TDB)	2027-01-01 00:00:00.000 (TDB)	2027-01-01 00:00:00.000 (TDB)	2027-01-01 00:00:00.000 (TDB)
SISEpos	20 m (2σ)	20 m (2σ)	13.43 m (3σ)	13.43 m (3σ)	13.43 m (3σ)
EIRP at boresight	25 dBW	14 dBW	26.7 dBW	26.7 dBW	26.7 dBW

The simulation of the PVT solution is based on the EKF framework presented in [15]. The simulation results are presented from Figure 7 through Figure 10. Figure 7 and Figure 8 respectively present the PVT error with and without using the DEM, while Figure 9 and Figure 10 respectively show the Dilution of Precision (DOP) with and without DEM. Due to the low number of satellites and the non-exhaustive optimization of the orbits (considering the relative phasing), the DOP is very high when no DEM data is used. A high DOP represents an ill-conditioned design matrix, which leads to a high covariance (and error) of the filter. To overcome the impact of the poor geometry (reflected by the high DOP), a solution is adopted where the LANS observables are complemented by DEM-based height measurements. Comparing Figure 8 (without DEM) to Figure 7 (with DEM), a large improvement can be observed.

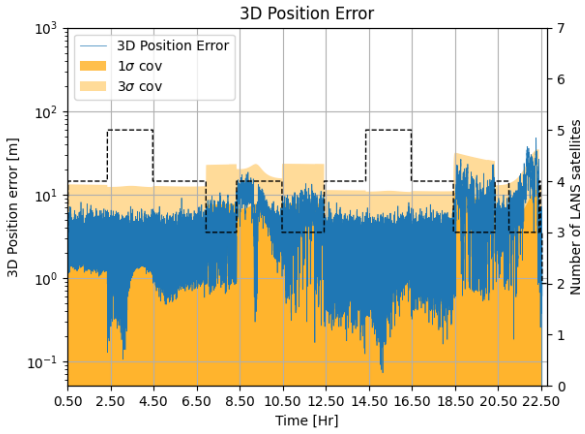

Figure 7 - 3D position error with DEM.

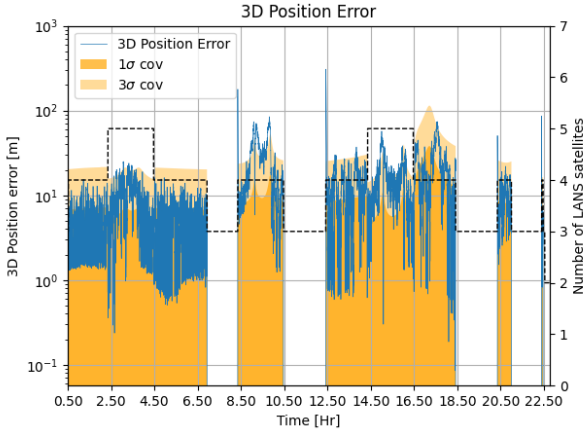

Figure 8 - 3D position error without DEM.

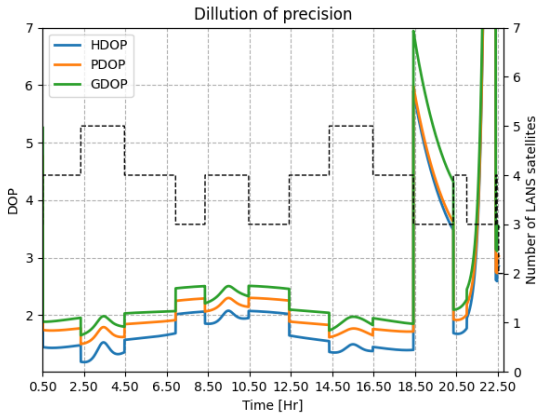

Figure 9 - DOP and visibility in the scenario with DEM.

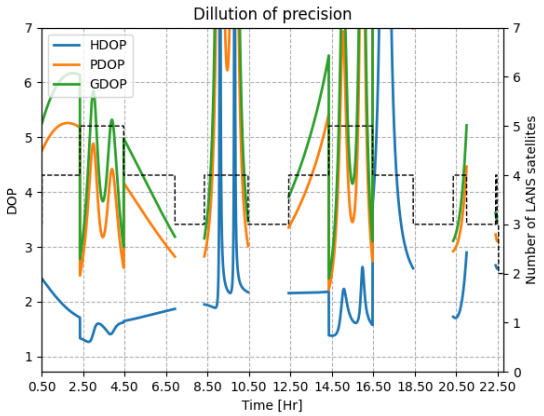

Figure 10 - DOP and visibility in the scenario without DEM.

As shown in Table 4, it can be concluded that the interoperability mission should be able to validate the performances of the system with a position accuracy in the order of 4.2 and 13.5 meters (68th percentile) respectively with and without using DEM measurements.

A third scenario was considered where the PVT accuracy was determined by assuming the use of a DEM and assuming that the SISE for all LNSP nodes would be 20 meters (95th percentile). This scenario would represent the case where each LNSP complies with the SISE expected value set within the AFS specification (AD-1 Volume A to LNIS [2]). In this scenario, the SISE is assumed to follow a normal distribution with an average value of 10 meters and with a standard deviation of 1 meter. The corresponding results are presented in Figure 11 and Table 4. In this case, the results are degraded (as expected) with respect to the nominal scenario (where the SISE of the NASA LCRNS nodes is improved). In this case, the PVT algorithm cannot achieve a position accuracy better than 10 meters (3σ).

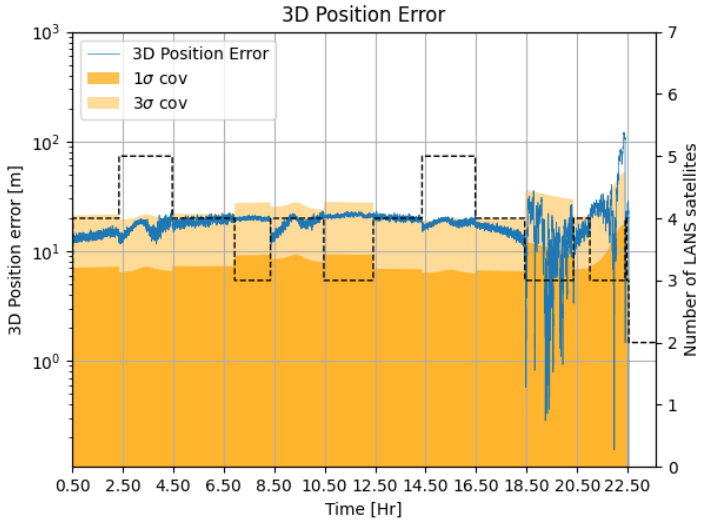

Figure 11 - 3D position results for the minimum required SISE scenario.

Complementary to AFS/LANS, LunaNet PNT services can also be provided through point-to-point (P2P) links. In this case, a ranging session would be initialized by the LNSP node, while the user node would turn around the signal (either regeneratively or non-regeneratively) allowing the LNSP node to derive so-called Two-Way Measurements (TWMs). The three NASA LNSP nodes will be equipped with a payload enabling the generation of TWMs to further enhance the position estimation. The general framework of the two-way measurements for a lunar constellation is presented in [16]. The main assumptions are presented below. Figure 12 shows a schematic view of a TWM. Conceptually, the LNSP node sends a signal to the user terminal which is then returned to the satellite that computes the observables. The observables are then forwarded to the user.

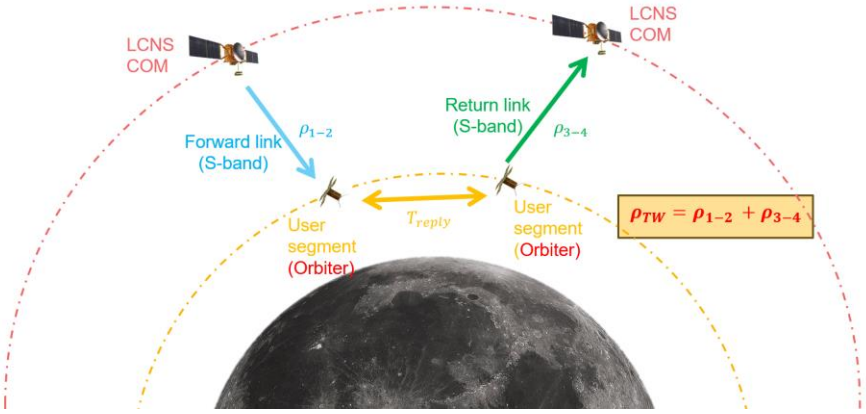

Figure 12 - Two-Way Measurement (TWM) diagram.

The TWM is modelled by Equation (2), where b_r represents the unmodelled receiver hardware biases, while η represents the ranging error due to the thermal noise observed on the observable. The system contribution to the TWM is captured by the $TWM - SISE_{pos}$ for the position domain and the $TWM - SISE_{vel}$ for the velocity domain, whose expressions are presented in equations (3) and (4) respectively.

$$\hat{\rho}_{TW} = \rho_{TW} + b_r + \eta \tag{2}$$

$$TWM - \mathrm{SISE}_{\mathrm{pos}} = \sqrt{(x - \tilde{x})^2 + (y - \tilde{y})^2 + (z - \tilde{z})^2 + (b_{HW}c)^2 + (b_{ts}|\vec{v}_{sat}|)^2} \tag{3}$$

$$TWM - \mathrm{SISE}_{\mathrm{vel}} = \sqrt{\left(\dot{x} - \tilde{\dot{x}}\right)^2 + \left(\dot{y} - \tilde{\dot{y}}\right)^2 + \left(\dot{z} - \tilde{\dot{z}}\right)^2 + \left(\dot{b}_{HW} c\right)^2 + \left(b_{ts} |\vec{a}_{sat}|\right)^2} \quad (4)$$

Here, x, y, z represent the true position of the satellites on the three axes of the used frame, while the tilde notation denotes the estimated satellite position as provided to the user. The dotted variables (e.g., $\dot{x}$) represent the velocity component for each axis. For the simulation of those quantities (e.g., $TWM - SISE_{pos}$), the same approach as for the one-way simulation is used as the same satellite has both the one-way and two-way measurement capability (except that the clock contribution is not modelled). Finally, b_{HW} represents the calibration residual error of the LNSP node. A typical value used is 5 ns. b_{ts} represents the timestamping bias of the satellite payload. A typical value used is 2 ns (which when multiplied with the satellite velocity represents a negligible quantity but is still included in the modelling used for the simulation).

Assuming the TWMs are generated by the communication payload of the LNSP node (and thus require a P2P link), it is not possible to have continuous access to these measurements as the available bandwidth needs to be balanced among various users and the data relay capability. For this reason, within this study it is assumed that only 12 minutes of TWM are available per hour. Regarding the specific schedule, two scenarios were assessed. The first scenario considers that the three satellites can perform the TWM session with the user simultaneously (which implies a very complex user terminal and is unlikely). The second scenario considers that none of the sessions from the three satellites overlap. The results are presented in Figure 13 and Figure 14 for the synchronized (i.e., sequential) and simultaneous (i.e., parallel) approach respectively, while the resulting DOP and visibility for the synchronized mode is shown in Figure 15. In these simulations, the altitude estimation by using a DEM is always considered in the filter. In these figures, TWM unavailability is marked by a vertical red line. For readability reasons, only half a day of results are plotted. However, a full day simulation was conducted with similar performances during both parts of the day.

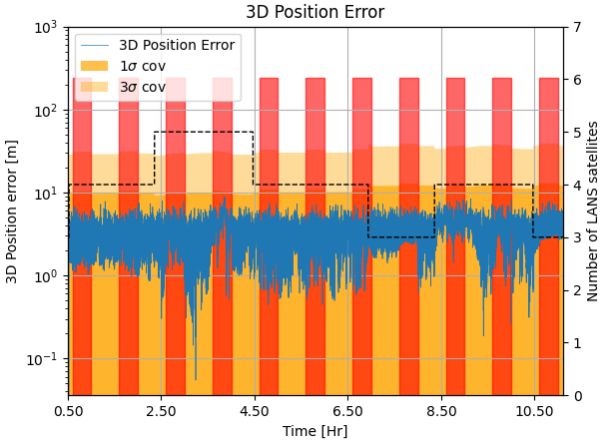

Figure 13 - 3D position results for the synchronized TWM schedule.

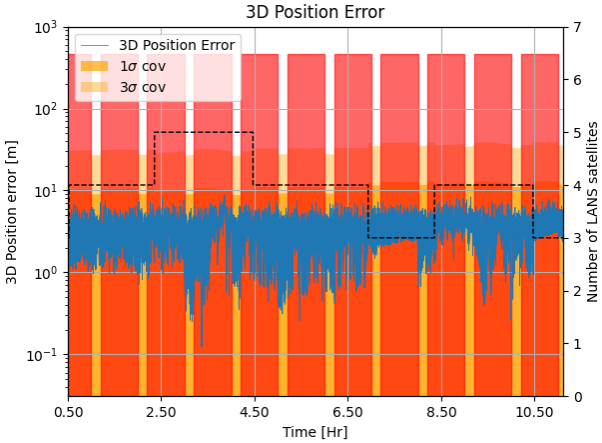

Figure 14 - 3D position results for the simultaneous TWM schedule.

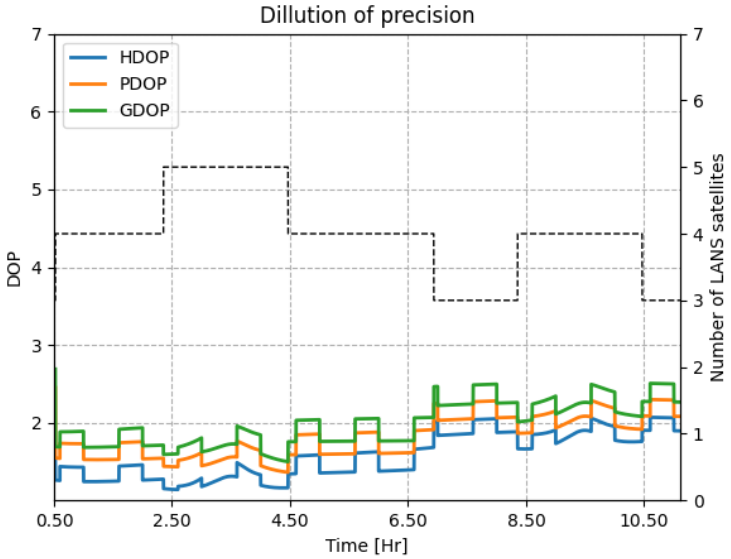

Figure 15 - DOP and visibility for the synchronized TWM schedule.

From this simulation, it is possible to conclude that the TWMs provide a benefit by slightly improving the position of the user. This is clearly shown in Figure 13. When the two-way measurements are available, the DOP value drops. From Table 4, the improvement can be noticed as well. However, as the LANS based PVT already provides good performance, the additional improvement realized by TWM is small. Additionally, both scheduling methods provide similar performances. It should be noted that the statistics in Table 4 cover the full analysis period and are not representative of the achievable instantaneous performance (due to large DOP variations and satellites visibility etc. across the period).

Table 4 - Results of the PVT analysis assuming a MiniRAFS.

	Mean 3D position error [m]	**68th percentile 3D position error [m]**
LANS	13.24	13.49
LANS + DEM	4.31	4.21
LANS + DEM (degraded SISE)	18.53	19.64
LANS + TWM simultaneous	3.70	3.67
LANS + TWM synchronized	3.62	3.63

5.3. GNSS Time Transfer

As shown in [6], using GNSS for PVT at lunar altitudes is challenging due to the high DOP as the GNSS satellites appear from a small angular region as seen by the lunar user. However, when the location of the demonstration lander is well known through other tracking techniques (DWE, DDOR, and laser ranging), GNSS can be used for time transfer, which could be a method to benchmark the LANS timing solution. Section 5.3.1 will further detail the assumptions for the GNSS time transfer analysis, while Section 5.3.2 provides some initial simulated performances of GNSS time transfer.

5.3.1. GNSS Time Transfer Model

For the purpose of this analysis, the demonstration lander is assumed to be equipped with a high-sensitivity GNSS receiver with an acquisition and tracking threshold of 18 dB-Hz. Two types of GNSS antenna configurations have been considered in this analysis. The first type consists of a directional high-gain antenna (HGA) with a boresight gain of 16 dBi, which is mounted on an antenna pointing mechanism (APM) that tracks the mean Earth direction. The second configuration considers the use of a low-gain antenna (LGA) which is assumed to have a gain of 5 dBi instead. The GNSS receiver configuration is shown in Table 5.

Table 5 - GNSS receiver configuration for the demonstration lander.

Parameter	Value/Configuration
Demonstration Mission Location	90 degrees South / 0 degrees East
Signals Used	E5a+L5
Observables	Pseudorange
Receiver Boresight Gain	High Gain: 16 dBi Low Gain: 5 dBi
Receiver Equivalent Noise Temperature	High Gain: 317 K Low Gain: 227 K
DLL Coherent Integration Time	20 ms
DLL Loop Bandwidth	0.1 Hz
Early-Late Spacing	1 chip

In this analysis, E5a/L5 signals are selected over E1/L1 signals due to their larger bandwidth and thus lower DLL tracking jitter. Furthermore, the Galileo-GPS timing offset (GGTO) must be taken into account since observations from both constellations are used. Here, it is assumed that the GGTO can be used as a correction to align the two timescales. The demonstration lander is situated at the South Pole for this analysis; however, any location on the near side of the Moon could be selected, which is not expected to have a significant impact on the time transfer results. In fact, the higher the latitude, the longer the period of (near) continuous GNSS visibility over the duration of a full month, which can be related to the lunar librations, as will be discussed in the following section.

The following receiver characteristics are set based on internal studies. For the high-gain configuration, the receiver equivalent noise temperature is set to 317 K assuming an antenna noise temperature of 187 K, an LNA with a gain of 29.5 dB and a noise figure of 1.4 [11]. For the low-gain configuration, a receiver equivalent noise temperature of 227 K was considered, with an antenna noise temperature of 34 K, and an LNA gain of 25.0 dB and noise figure of 0.35. The DLL loop filter parameters are also shown in Table 5. Within this study, both the OCXO and MiniRAFS clocks are considered. Their respective behavior was modelled using the Allan deviations that are shown for each clock in Table 6.

Table 6 - Allan Deviation for OCXO and MiniRAFS.

Averaging time	OCXO	MiniRAFS
$\tau = 1$ s	8.5e-11	2e-11
$\tau = 10$ s	8e-11	5e-12
$\tau = 100$ s	8e-11	2e-12
$\tau = 1{,}000$ s	1e-10	8e-13
$\tau = 10{,}000$ s	6e-10	6e-13
$\tau = 100{,}000$ s	6e-09	8e-13

The configuration of the GNSS simulation is shown in Table 7. The Galileo constellation is constructed based on the almanac parameters obtained on 2025-04-11, and the YUMA almanac published for Week 311 (in 2025) is used for GPS. The analysis is conducted for a 7-day period from 10 June 2026 to 17 June 2026. Since this period is in the future at the time of writing, GNSS satellite orbit and clock errors have been simulated according to the method described in Section 5.2, with the same settings provided in [13]. Furthermore, the location of the lander is assumed to be known perfectly, which is an optimistic assumption that needs to be refined in future work.

Table 7 - GNSS simulation configuration.

Parameter	Value/Configuration
Simulation Period	10-17 June 2026 (7 days)
Galileo Constellation	Almanac 2025-04-11 (27 satellites) [17]
GPS Constellation	YUMA Almanac Week 311 (2025) (31 satellites) [18]
SISE (position and velocity)	Modelled as First-Order Gauss-Markov process [13]
Lander position error	0 meter
Error Modelling	DLL thermal noise

The synthetic pseudorange measurements for each constellation S are generated according to the model shown in Equation (5). This includes the simulated "true" geometric range (accounting for light time delay) between the GNSS satellite (position denoted by $\tilde{x}_{sat}$) and demonstration lander (position denoted by $\tilde{x}_{rx}$) in meters with $||\cdot||$ denoting the operator for the Euclidean norm, the receiver clock offset (Δt_{rx}), the satellite clock offset (Δt_{sat}), and the GGTO-correction error (ε_{GGTO}) in seconds, and the DLL thermal noise (η_{DLL}) in meters. The thermal noise is modelled as a normally distributed variable with zero-mean and a standard deviation σ_{DLL}. σ_{DLL} is calculated as a function of the received C/N_0 and receiver configuration (as specified in Table 5), as shown in [15] and based on [11]. Furthermore, Galileo System Time (GST) is selected as the reference timescale for this analysis. As mentioned, it is assumed that the GPS measurements can be aligned to GST by using the GGTO correction. This correction would have a certain error, which is modelled here as a normally distributed variable with zero mean and a standard deviation σ_{GGTO} of 2.0 ns. Accordingly, as shown on the right side of Equation (5), this GGTO-correction error is only applied to the GPS measurements. Lastly, the term c represents the speed of light in m/s.

$$\rho^S = ||\tilde{x}_{sat} - \tilde{x}_{rx}|| + c\,(\Delta t_{rx} - \Delta t_{sat} + \varepsilon_{GGTO}) + \eta_{DLL} \qquad \text{where} \quad \varepsilon_{GGTO} = \begin{cases} 0, & S = GAL \\ \mathcal{N}\sim(0, \sigma^2_{\mathrm{GGTO}}), & S = GPS \end{cases} \tag{5}$$

The following additional assumptions have been considered in this analysis. Firstly, as the Moon only has an exosphere, errors due to atmospheric effects are neglected. Additionally, a grazing altitude of 1000 km above the Earth surface has been considered, meaning that measurements coming from GNSS satellites passing below this altitude as seen from the perspective of the lunar lander have also been discarded to further allow for neglecting the atmospheric effects. Furthermore, additional errors due to group delays and multipath effects have not yet been considered in this work.

The estimation of the receiver clock offset to the reference timescale (Galileo System Time) can be described as follows. As shown in Equation (6), the offset between the receiver clock and Galileo System Time (Δt_{rx}) can be expressed as a function of the observed pseudorange (ρ^S), and the values of the satellite position ($\hat{x}_{sat}$), the lander position ($\hat{x}_{rx}$), and the satellite clock offset (Δt_{sat}) as known to the user.

$$\Delta t_{rx} = t_{rx} - t_{ref} = \frac{1}{c}\left[\,\rho^S - ||\,\hat{x}_{sat} - \hat{x}_{rx}\,||\,\right] + \Delta t_{sat} \tag{6}$$

In practice, this analysis was conducted using the same tool as in Section 5.2, but employing a Weighted Least Squares implementation instead. The Least Squares problem to be solved can be formulated as:

$$\boldsymbol{y} = H\boldsymbol{x} + \boldsymbol{\epsilon} \tag{7}$$

Here, $\boldsymbol{y}$ is the m-size vector of observed minus computed pseudorange observations for m satellites at a given epoch and $\boldsymbol{\epsilon}$ is the m-size vector of corresponding residual errors. Since the receiver clock offset is the only unknown, the state vector $\boldsymbol{x}$ to be estimated consists of one parameter: $\boldsymbol{x} = [\Delta t_{rx}]$. As this parameter is already linearly related to the observation equation, the Least Squares method can readily be performed, with the design matrix formulated as: $H = c\,\mathbf{1}_{m\times 1}$. Accordingly, the estimated receiver clock offset is found from the Weighted Least Square (WLS) solution as shown in Equation (8). The weights in the weight matrix W are calculated as the inverse of the measurement covariance matrix, as defined in [15]. Here, the covariance for each measurement consists of the sum of the variance of the thermal noise (σ^2_{DLL}), and the satellite position and clock uncertainties computed as the variance of their respective first-order Gauss-Markov processes.

$$\hat{\boldsymbol{x}} = \Delta\hat{t}_{rx} = (H^{\mathsf{T}}WH)^{-1}\,H^{\mathsf{T}}W\,\boldsymbol{y} \tag{8}$$

In this analysis, this WLS estimation was performed at epochs spaced by 30 seconds, for each epoch with a sufficient number of measurements (which in this case is only one, given the single unknown parameter). In an effort to further improve the error of the estimated receiver clock offset, a smoothing method similar to the Common GNSS Generic Time Transfer Standard (CGGTTS) [19] is employed. Every 16 minutes, a batch of 26 estimates (from the WLS solutions performed every 30 seconds) are gathered to perform a linear fit. These 26 estimates correspond to the first 13 minutes of the 16-minute window, while the remaining 3 minutes are neglected, which is done in line with the CGGTTS. The linear fit is then performed for the center epoch of the 13 minutes.

5.3.2. GNSS Time Transfer Performance

At and near the lunar South Pole, the visibility of the GNSS constellations has an approximately monthly cycle due to the lunar librations, which cause the Earth to disappear below the local horizon for 1 to 2 weeks at a time. Figure 16 and Figure 17 show the visibility for the Galileo and GPS constellations respectively over the month of June 2026 as seen by the demonstration lander using the previously described high-gain configuration. Here, it can be seen that the GNSS visibility starts with a period of zero satellites in view, which increases as the Earth rises above the horizon, and then later in the month decreases again once the Earth sets below the horizon. For this analysis, the 7-day period of 10 to 17 June 2026 was chosen, since the Earth is continuously fully above the horizon and in view of the demonstration lander. It can also be noted that the elevation angle of the Earth and the GNSS satellites remains quite low for the entire visibility period, namely around 10-12 degrees at most. This indicates that multipath could potentially have a noticeable impact on the GNSS performance, though this effect has not yet been considered in this work.

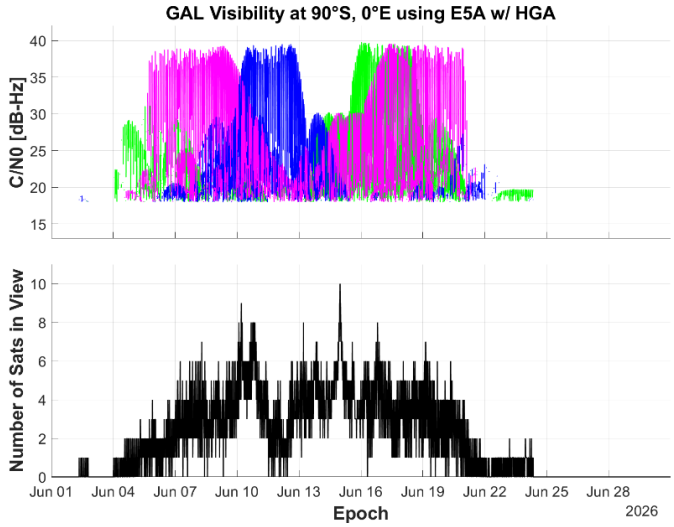

Figure 16 - C/N_0 and visibility of Galileo satellites tracked by the demonstration lander.

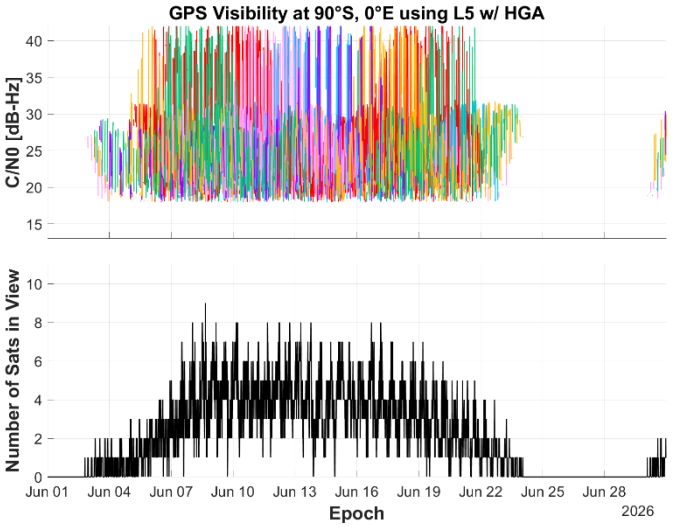

Figure 17 - C/N_0 and visibility of GPS satellites tracked by the demonstration lander.

Figure 16 and Figure 17 also show the carrier-to-noise density ratio (C/N_0) for the Galileo and GPS satellites respectively, where each color represents the individual orbital planes within the constellations. Here, it can be noticed that the magnitude of the C/N_0 is varying over the period for each of the planes. This is related to whether the GNSS satellites are tracked through their main or secondary lobes, which in turn depends on the relative orientation of each plane with respect to the lunar user. This relative orientation is also changing in time as the Moon travels along its orbit around the Earth, which can for example be seen in Figure 18 and Figure 19.

Since the transmitters on the GNSS satellites are oriented towards the center of the Earth, the main lobes are mainly observed when the orbital plane is more in line with the Moon-Earth direction and the GNSS satellites pass "behind" the Earth, such as the blue orbit in Figure 18. When the orbital plane moves more towards being perpendicular to the Moon-Earth direction, the GNSS satellites are tracked through their side lobes instead. This is possible until the plane is almost fully perpendicular and the secondary lobes can no longer be tracked either, such as the blue orbit in Figure 19. This leads to periods of no visibility for certain planes, until they start rotating to be more in line with the Moon-Earth direction again. This can affect the overall visibility, such as around June 12-13 for Galileo, where the total number of satellites in view is lower since it is mainly tracking satellites from the blue plane and less so from the other two planes. GPS seems to have a more balanced visibility since it has six orbital planes in total. It should also be noted that these simulations are based on a GPS almanac from March 25th, 2025, where not all GPS satellites were transmitting on L5 as yet, namely only 18 out of the 31 GPS satellites as of that date.

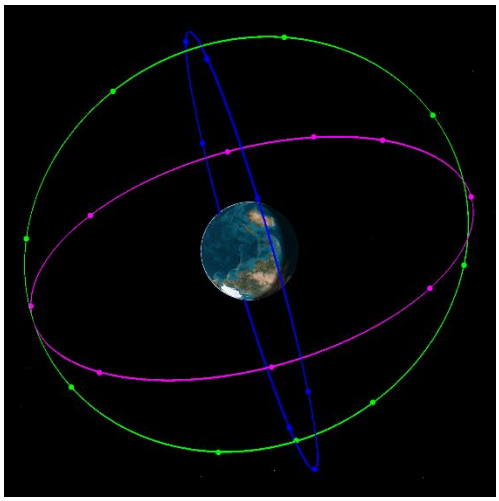

Figure 18 - Orientation of Galileo orbital planes as viewed from the lunar South Pole on 12 June 2026.

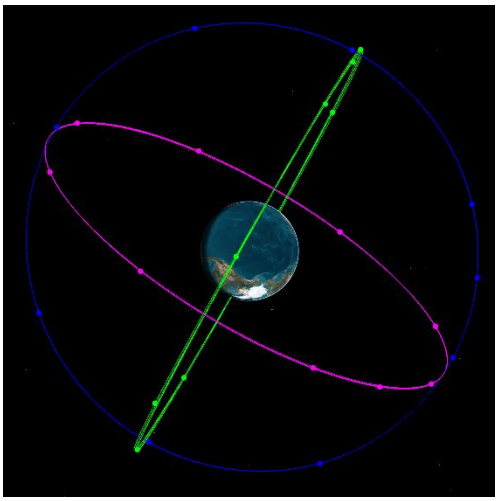

Figure 19 - Orientation of Galileo orbital planes as viewed from the lunar South Pole on 17 June 2026.

The GNSS time transfer results using the high-gain configuration are presented first, where the corresponding GNSS visibility for the considered 7-day period is shown in Figure 20, with an average number of total GNSS satellites in view of 8.3 for this period. Figure 21 shows the clock error results for the MiniRAFS, where this error is computed as the difference between the estimated receiver clock offset and the simulated "true" receiver clock offset. Here, the clock error of the instantaneous solution obtained every 30 seconds is shown in blue and the clock error of the 16-minute linear-fit batches is shown in orange. The standard deviation of error of the 30-second solution is 0.86 ns, while for the 16-minute solution this is suppressed to 0.28 ns. The corresponding overlapping Allan deviations of the estimated receiver clock offsets are shown in Figure 22, along with the Allan deviation of the true clock shown in green. At shorter averaging times, the 30-second solution has a higher Allan deviation than the true clock, indicating that GNSS time transfer may be less suitable to "validate" the true clock offset of a MiniRAFS on the Moon in real time. This is improved by the 16-minute linear fit, which seems to attenuate not only the noise of the GNSS observations, but also the noise of the clock itself. However, due to the lower sampling rate, this solution cannot be used to assess the very short-term stabilities. In the longer averaging times, both estimated solutions seem to "catch up" to the true noise floor of the MiniRAFS clock.

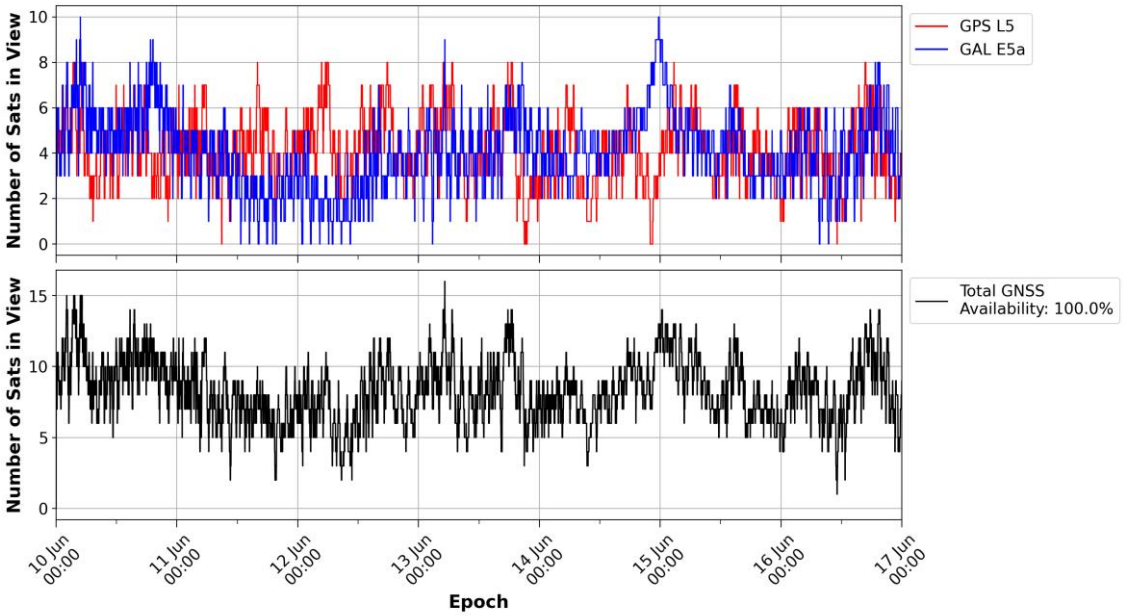

Figure 20 - GNSS visibility of the demonstration lander with the high-gain configuration.

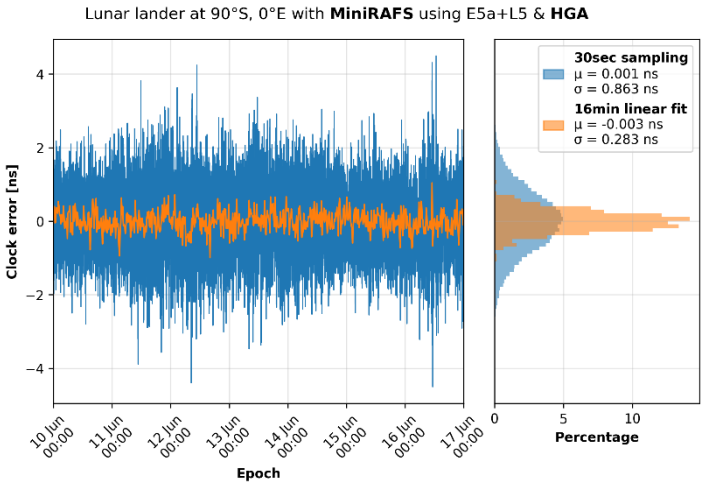

Figure 21 - Estimated receiver clock offset error when using a MiniRAFS and the high-gain configuration.

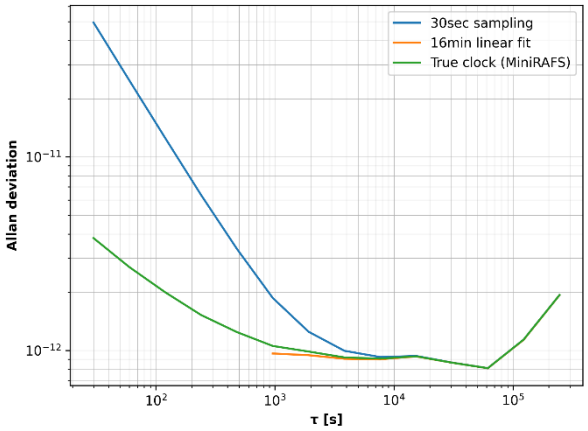

Figure 22 - Estimated and true MiniRAFS overlapping Allan deviation when using the high-gain configuration.

The results for the receiver clock estimation using the high-gain configuration for an OCXO onboard the demonstration lander are shown in Figure 23. Here, only the 30-second estimation is presented, as the 16-minute linear fit method was not found to be suitable for capturing the true OCXO behavior. The standard deviation of 0.86 ns is similar to that of the 30-second solution of the MiniRAFS, though the mean is an order of magnitude higher. In turn, the overlapping Allan deviation for the estimated receiver clock offset of the OCXO is quite close to that of the true clock at all averaging times, as shown in Figure 24.

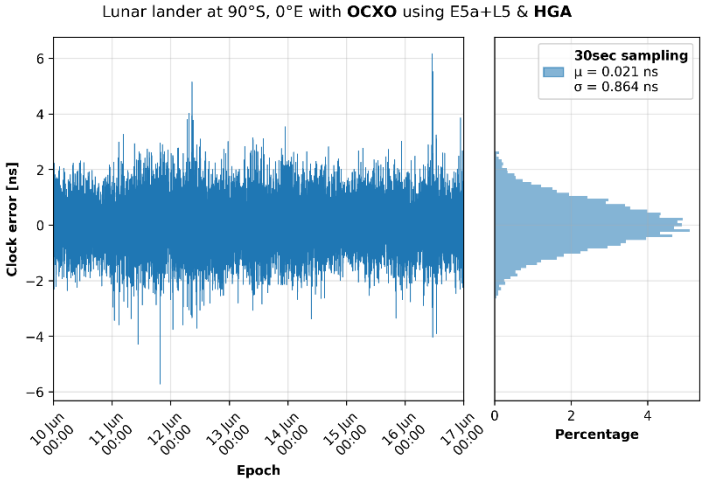

Figure 23 - Estimated receiver clock offset error when using an OCXO and the high-gain configuration.

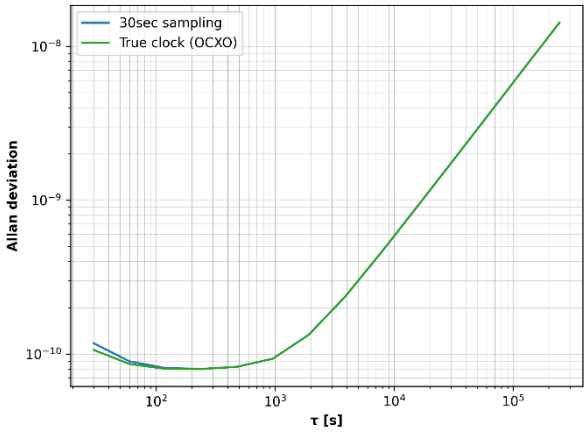

Figure 24 - Estimated and true OCXO overlapping Allan deviation when using the high-gain configuration

Next, the results for the receiver clock offset estimation using the low-gain configuration described in the previous section will be presented. In this configuration, the receiver antenna gain is lower, which results in a lower number of GNSS satellites that are tracked by the receiver as compared to the previously shown high-gain configuration, as shown in Figure 25. Here, the average number of total GNSS satellites in view is only 2.5 over the considered 7-day period. Furthermore, the high-gain configuration had 100% GNSS satellite visibility, which in this case means that at least 1 GNSS satellite is in view at all times. Meanwhile, with this low-gain configuration, there are intermittent periods where no GNSS satellites are tracked, in this case resulting in about 93% availability over the 7-day period. In practice, one could linearly interpolate the receiver clock estimate during these gaps, though this is not considered in this work. Lastly, using the low-gain configuration would also provide a lower C/N_0 as compared to the high-gain configuration, resulting in not only fewer, but also noisier measurements.

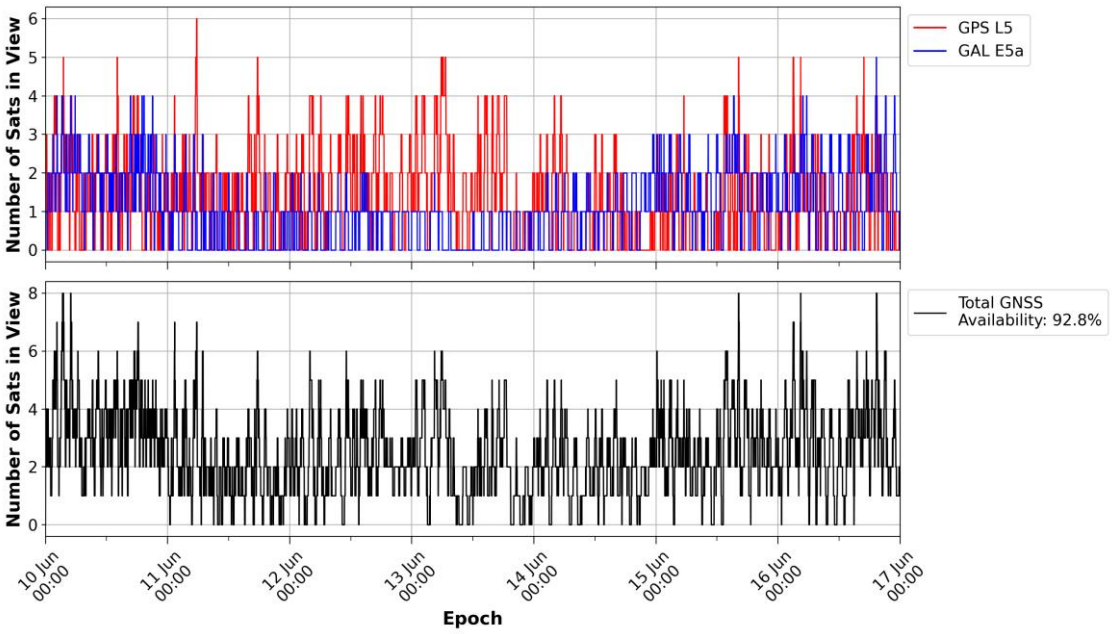

Figure 25 - GNSS visibility of the demonstration lander with the low-gain configuration.

The errors for the receiver clock offset estimation when using the low-gain configuration are presented in Figure 26 and Figure 27 for the MiniRAFS and the OCXO respectively. The standard deviation of the 30-second solution is around 2.3 ns for both of the clocks. This is a higher error than for the high-gain result, which is as expected due to the lower number of satellites, though it is still in the order of nanoseconds. For the MiniRAFS, the result for the 16-minute linear fit is also included, achieving a standard deviation of around 0.5 ns. However, the availability of this solution is slightly lower at 86%, since the 16-minute windows with any gaps in the 30-second solution were not considered.

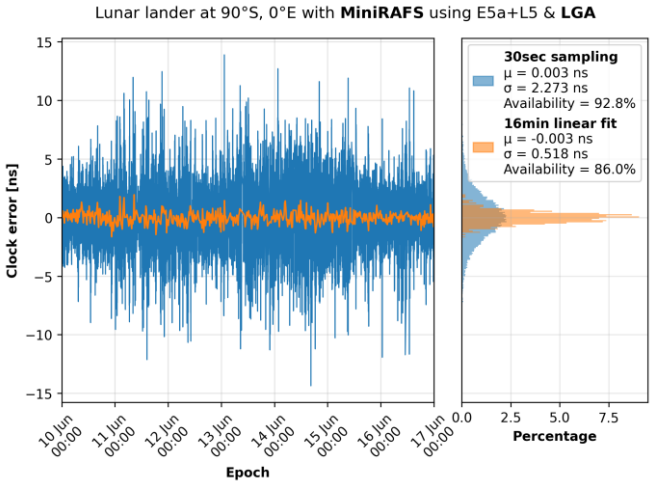

Figure 26 - Estimated receiver clock offset error when using a MiniRAFS and the low-gain configuration.

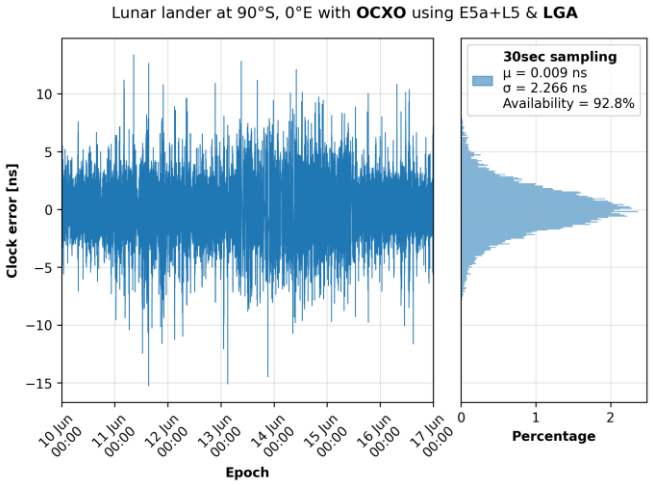

Figure 27 - Estimated receiver clock offset error when using an OCXO and the low-gain configuration.

The reader is reminded that this analysis represents an optimistic result, as the following potentially significant errors have not been considered as yet. This includes the achievable lander position accuracy, which has been discussed in Section 5.1. Furthermore, there can also be a difference in group delays, this depends on which frequencies will ultimately be used for the GNSS time transfer and if these are different than the reference signals of the satellite clock products that will be used. Lastly, the effects of multipath are not well known as yet for lunar surface users and could potentially have a significant impact for lunar South Pole users considering the low elevation angles of the GNSS satellites in view.

6. CONCLUSIONS

The LANS demonstration mission in 2029 is an excellent opportunity to exercise the LunaNet standards, systems, and user equipment in the operational lunar environment. ESA, NASA and JAXA all expect to have the first nodes in place for the demonstration mission allowing multi-lateral cross-validation approaches. This paper presents the current status of the LANS demonstration mission, including updates on potential payload configurations. We simulated the LANS-derived position, velocity, and timing (PVT) performance during the demonstration mission timeframe, incorporating one ESA LCNS node, three NASA LCRNS nodes, and one Japanese LNSS node. To overcome the limitation of high DOP (due to the constellations not being fully complete, as well as the relative phasing that was not optimized), digital elevation measurements (from LOLA maps) are used to vertically constrain the user position. The initial simulations show that a static user on the lunar South Pole could achieve below 10m positioning accuracy with the expected 5-satellite LANS constellation and with the DEM measurements further increasing the performance. In addition, initial analysis has shown that a reference position may be computed in post-processing at less than 1m uncertainty (increasing to ~1m when considering reference frame errors) and a reference user clock may be estimated to a few ns using GNSS time transfer. Future work will focus on refining these time transfer results by accounting for position knowledge errors, LANS to GNSS time calibration errors, and multipath effects.

REFERENCES

[1] D. Israel, L. V. Cooper, K. Mauldin and K. Schauer, "LunaNet: A Flexible and Extensible Lunar Exploration Communications and Navigation Infrastructure and the Inclusion of SmallSat Platforms," in *34th Annual Small Satellite (SmallSat) Conference*, Utah, 2020.

[2] C. G. Manning, "LunaNet Interoperability Specification," NASA, February 2023. [Online]. Available: https://www.nasa.gov/directorates/somd/space-communications-navigation-program/lunanet-interoperability-specification/. [Accessed 1 September 2025].

[3] NASA, "NASA's Moon to Mars Strategy and Objectives Document," NASA, Washington, 2023.

[4] M. Murata, I. Kawano and S. Kogure, "Lunar Navigation Satellite System and Positioning Accuracy Evaluation," in *2022 International Technical Meeting of the Institute of Navigation*, Long Beach, California, 2022.

[5] C. Gramling, J. Crenshaw, M. Murata, R. Swinden, F. Melman, C. Stallo and J. Ventura-Traveset, "Towards LunaNet Lunar Augmented Navigation Service (LANS) Interoperability Demonstration and Monitoring," in *Proceedings of the 18th International Conference on Space Operations (SpaceOps 2025)*, Montreal, 2025.

[6] A. Delépaut, P. Giordano, J. Ventura-Traveset, D. Blonski, M. Schönfeldt, P. Schoonejans, S. Aziz and R. Walker, "Use of GNSS for lunar missions and plans for lunar in-orbit development," *Advances in Space Research,* vol. 66, no. 12, pp. 2739-2756, 2020.

[7] Orolia, "iSpace+ miniRAFS Spec," 18 January 2021. [Online]. Available: https://cdn.everythingrf.com/live/Spectratime_miniRAFS_Spec_01_19_21_1_637659903588188000.pdf. [Accessed 1 September 2025].

[8] Bliley Technologies Inc., "Iris Space OCXO for LEO & Small Satellite Applications," 2025. [Online]. Available: https://resources.bliley.com/iris-space-ocxo-leo-constellations-small-satellites. [Accessed 12 September 2025].

[9] J. Chabé, C. Courde, J.-M. Torre, S. Bouquillon, A. Bourgoin, M. Aimar, D. Albanèse, B. Chauvineau, H. Mariey, G. Martinot-Lagarde, N. Maurice, D.-H. Phung, E. Samain and H. Viot, "Recent Progress in Lunar Laser Ranging at Grasse Laser Ranging Station," *Earth and Space Science,* vol. 7, 2020.

[10] A. R. N. &. S. K. Fienga, "Lunar References Systems, Frames and Time-scales in the context of the ESA Programme Moonlight.," *arXiv,* vol. preprint arXiv:2409.10043., 2024.

[11] E. D. Kaplan and C. Hegarty, Understanding GPS/GNSS: principles and aplications, Artech house, 2017.

[12] M. Di Benedetto, G. Boscagli, F. De Marchi, D. Durante, F. Santi, A. Sesta, M. Plumaris, A. Fienga, N. Linty, K. Sosnica, J. Belfi and L. Iess, "An architecture for a lunar navigation system: orbit determination and time synchronization," in *Proceedings of the ESA's 8th International Colloquium on Scientific and Fundamental Aspects of GNSS*, 2022.

[13] E. Gallon, M. Joerger and B. Pervan, "Robust Modeling of GNSS Orbit and Clock Error Dynamics," *NAVIGATION: Journal of the Institute of Navigation,* vol. 69, no. 4, 2022.

[14] M. K. Barker, E. Mazarico, G. Neumann, M. Zuber, J. Haruyama and D. Smith, "A new lunar digital elevation model from the Lunar Orbiter Laser Altimeter and SELENE Terrain Camera," *Icarus,* pp. 346--355, 2016.

[15] Y. Audet, F. T. Melman, S. Molli, A. Sesta, M. Plumaris, D. Psychas, R. Swinden, P. Giordano and J. and Ventura-Traveset, "Positioning of a Lunar Surface Rover on the South Pole Using LCNS and DEM," *Advances in Space Research, 74,* pp. 2532-2550, 2024.

[16] Y. Audet, F. T. Melman, S. Petri, J. Oduber, B. Wadsworth, R. Swinden, C. Stallo, D. Pettitt and J. Ventura-Traveset, *Introducing Two-Way Measurements for Lunar Navigation with Moonlight Initial Operational Capability,* Wroclaw, 2025.

[17] European GNSS-Service Centre (GSC), "Galileo Almanac," 11 April 2025. [Online]. Available: https://www.gsc-europa.eu/gsc-products/almanac. [Accessed 11 April 2025].

[18] U.S. Coast Guard Navigation Center (NAVCEN), "GPS Almanac Archive," 25 March 2025. [Online]. Available: https://www.navcen.uscg.gov/archives. [Accessed 2025 March 2025].

[19] P. D. a. G. Petit, "CGGTTS-Version 2E: An extended standard for GNSS time transfer," *Metrologia,* vol. 52, no. 6, 2015.